Subpercent-Scale Control of 3D Low Modes of Targets Imploded in Direct-Drive Configuration on OMEGA

D. T. Michel, I. V. Igumenshchev, A. K. Davis, D. H. Edgell, D. H. Froula, D. W. Jacobs-Perkins, V. N. Goncharov, S. P. Regan, A. Shvydky, and E. M. Campbell

Phys. Rev. Lett. **120**, 125001 — Published 23 March 2018

DOI: 10.1103/PhysRevLett.120.125001

Subpercent-scale control of 3-D low-modes of targets imploded in direct-drive configuration on OMEGA

D. T. Michel,* I. V. Igumenshchev, A. K. Davis, D. H. Edgell, D. H. Froula, D. W. Jacobs-Perkins, V. N. Goncharov, S. P. Regan, A. Shvydky, and E. M. Campbell

Laboratory for Laser Energetics, University of Rochester, Rochester, NY 14636

(Dated: February 21, 2018)

Abstract

Multiple self-emission x-ray images were used to measure tomographically target modes 1, 2, and 3 up to the end of the target acceleration in direct-drive implosions on OMEGA. Results show that the modes consist of two components: the first varies linearly with the laser beam-energy balance and the second is static and results from physical effects including beam mistiming, mispointing, and uncertainty in beam energies. This was used to reduce the target low-modes of low-adiabat implosions from 2.2% to 0.8% by adjusting the beam-energy balance to compensate these static modes.

PACS numbers:

Keywords:

In laser-driven implosion experiments, a laser illuminates a spherical target which leads to the ablation and target acceleration through the rocket effect. This method is widely used to study plasma physics [1] including high-energy-density physics [2–4] and inertial confinement fusion (ICF) [5, 6]. In all cases, maintaining spherical symmetry throughout the implosion is critical to obtaining a one-dimensional behavior that maximizes the internal energy of the hot-spot plasma at final compression. In ICF experiments, a capsule filled with deuterium (D) and tritium (T) is imploded to create a self-sustained fusion burn to produce a net energy gain. Several simulations and comparisons with experiments have shown that target low-mode nonuniformities lead to a severe reduction in the implosion performance because of increased residual kinetic energy during stagnation and uneven compression, resulting in reduced hot-spot pressure and truncated burn [7–10]. This degradation was shown to be significant for modes $l \leq 3$, where l is the order of the modes of the spherical harmonic decomposition of the target shape [9, 11]. Consequently, reducing low-mode nonuniformities has been identified as one of the critical steps in demonstrating ignition at the National Ignition Facility (NIF) [12–14], or conditions that are hydrodynamically equivalent to ignition when scaled from tens of kilojoules implosions on OMEGA to megajoule energies on the NIF [15–17].

Over the last decade, different experiments have shown that targets imploded with the current laser facilities experience significant growth of their low-mode nonuniformities. Mode $l = 1$ was typically inferred from properties of the final assembly including asymmetry in its areal density [18], variation of its ion temperature along different lines of sight [19], hot-spot motion [20], and asymmetric x ray emission of a Ti layer embedded at the inner surface of the shell [21]. Modes $l \geq 2$ were measured from the hot-spot shape [22, 23], x-ray [24] or Compton [25] radiography, x-ray absorption spectroscopy [26], and self-emission shadowgraphy [27].

Several studies have focused on the causes of the asymmetries and the development of methods to correct them. In indirect-drive ICF (where the laser light is converted into x rays before irradiating the target), the laser beam wavelength was modified to exploit cross-beam energy transfer and improve the spherical symmetry of the hot-spot emission [22, 23]. The improvement, however, was limited because the observable (i.e., the imploded hot-spot shape) was restricted to modes $l \geq 2$ and was too indirect to give accurate access to the three-dimensional (3-D) structure of the shell [11]. In direct-drive implosions (where the

laser directly irradiate the target) [6], simulations have identified different effects that create nonuniformities including beam pointing, beam timing, and beam-energy imbalance. Some experimental improvement of the beam-power balance was performed [28]. Success has been limited, however, in correcting all of them because of the difficulty in modeling and quantifying each effect [29].

This Letter reports the first experimental demonstration, in direct-drive implosions on OMEGA, that the target modes $l = 1$, 2, and 3 up to the end of the target acceleration are the result of two components; a dynamic part that varies linearly with the beam-energy balance modes, and approximately constant static modes. This result was used to reduce the total target modes $l = 1$, 2, and 3 from 2.3% to 0.8% in low-adiabat implosions by adjusting the beam-energy balance to compensate the static modes. Over three shots, the 3-D modes $l = 1$, 2, and 3 of the ablation-front surface of the imploding targets (called target modes) were tomographically recorded from four lines-of-sight. The projected ablation-front contours were measured with framing cameras using the x-ray self-emission shadowgraphy technique [27, 30]. The projected ablation-front motions were obtained by comparing the contour positions on the framing cameras with the corresponding contour positions measured on a nonimploding solid-CH-ball shot. Results show a linear variation of the target modes with the beam energy balance modes. The values of the low mode coupling coefficients (i.e. the linear factor for each l) decreased with l. This was due to the individual beam shape that modifies the laser illumination modes compared to the beam energy balance modes. The static modes, evaluated on low-adiabat implosions, exhibit dominant modes $l = 1$ as they experienced the largest coupling.

The experiments employed 60 ultraviolet (351 nm) laser beams at the OMEGA Laser System [31]. The beams illuminated the target and were smoothed by polarization smoothing [32], smoothing by spectral dispersion [33], and distributed phase plates (4.4-order super-Gaussian with 95% of the energy contained within 820-μm diameter) [34]. A 2-ns-long square pulse irradiated 866 ± 3-μm-diam., 19.2 ± 0.2-μm-thick, round CH capsules (1.03 g/cm^3 CH shells with mode amplitudes < 50 nm containing 17 ± 1.5 atm of D2) with an energy of 20.2 ± 0.4 kJ, resulting in an overlapped intensity $\sim 4.3 \times 10^{14}$ W/cm^2. The beam-energy balance was varied over three shots. An additional reference shot used a solid CH ball of 856-μm diameter. For each shot, two high-speed video cameras (1000 images per second) were used to automatically position the target at target chamber center within 1.5 μm.

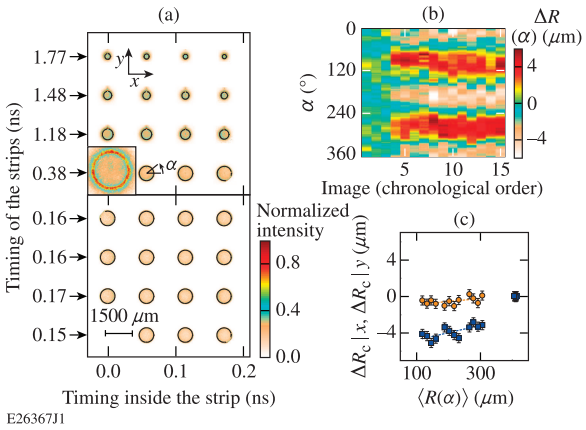

FIG. 1: (a) Comparison of the self-emission images recorded on the second capsule shot (upper figure) and the reference shot (lower figure). The black circles correspond to the inner edge contours of the intensity peak. The image timings are the addition of the timings of the strip and the timings inside the strip. The insert corresponds to the image recorded at 1.82 ns in the upper figure. (b) Evolution of the angular variation of the difference between the contour radius and the averaged contour radius $[\Delta R(\alpha)]$ for the images in the upper figure in (a). (c) Differences between the upper and the lower figures in (a) in the contour center positions for images at similar locations (i.e. recorded by the same pinhole) along x [orange circles $(\Delta R_c|_x)$] and along y [blue squares $(\Delta R_c|_y)$] as a function of the averaged contour radius $\{\langle R(\alpha)\rangle$[35]$\}$; x and y directions are indicated in (a). The error bars at the 90th percentile and the linear fits between 300 μm and 100 μm are plotted (dashed lines in corresponding colors).

Four x-ray framing cameras, located at different lines of sight, used arrays of 16 pinholes to get 40 ps (three cameras) and 200 ps (one camera) time-integrated images of the soft x rays emitted by the irradiated target on four horizontal strips of a microchannel plate (MCP) [36]. The cameras used magnifications of $M = 6$ (two cameras) and $M = 4$ (two cameras) with pinhole sizes of 10 μm and 15 μm resulting in point spread functions with full width at half maximum of $d_{\rm PSF} \approx 10$ μm and $d_{\rm PSF} \approx$ 15 μm, respectively [27]. On all cameras 25.4-μm-thick Be filters were used to record the x rays > 1 keV. For all imploding shells, the strip activations were timed to ~ 0.4 ns ~ 1.2 ns, ~ 1.5 ns and ~ 1.8 ns, whereas for the reference shots, they were synchronized to ~ 0.2 ns after the beginning of the laser pulse (defined as the 1% of the maximum intensity) [Fig. 1(a)]. The absolute image timings were known within ± 10 ps and the interstrip timings within ± 2.5 ps [27, 37]. For each

camera, the same pinhole array was used on all shots to maintain the distance between images.

Each self-emission image was used to measure the projection of the ablation-front surface on the diagnostic [30, 38] by tracking the inner edge contour of the intensity peak [Fig. 1(a)]. The recorded intensity was the strongest near the ablation front because the emitting plasma had the largest density and the integration distance of the emission was the longest. Just inside the ablation front, the recorded intensity dropped by a factor of 2 as the plasma became optically thick, absorbing its emission and the emission coming from the back of the target [insert in Fig. 1(a)]. The time integration and spatial convolution of the diagnostic induced inward shift of the inner gradient constant on each image. For each image, the angular variation of the difference between the projected ablation-front radius [$R(\alpha)$] and its average $\{\Delta R(\alpha) = R(\alpha) - \langle R(\alpha)\rangle$ where $\langle\rangle$ denotes the 2π angular average and α is the angle going counterclockwise relative to the horizontal [Fig. 1(a)]$\}$ was determined [Fig. 1(b)]. The contour center was determined iteratively by fitting the contour with a circle. To reduce the error, self-emission images were angularly averaged over 20°, which was larger than the radial convolution [$= (360/2\pi)d_{\rm PSF}/\langle R(\alpha)\rangle < 5°$] and smaller than the scale length of the modes studied here [$= 2\pi\langle R(\alpha)\rangle/l > 120°$]. The difference at an averaged radius of 150 μm $[\Delta R(\alpha)]_{150}$ and its associated error distribution [39] was obtained by linearly fitting the evolutions of $\Delta R(\alpha)$ with $\langle R(\alpha)\rangle$ ranging from ~ 300 μm to ~ 100 μm. The contour at 150 μm was deduced $[R(\alpha)]_{150} = 150\{1 + [\Delta R(\alpha)]_{150}\}$.

The projected motions of the ablation-front surface center during the implosion ($\Delta R_{\rm c} = \sqrt{\Delta R_{\rm c}|_x^2 + \Delta R_{\rm c}|_y^2}$ where $\Delta R_{\rm c}|_x$ and $\Delta R_{\rm c}|_y$ correspond to the horizontal and vertical projected motions) were obtained by measuring the differences in the corresponding contour center positions (i.e. recorded by the same pinhole) between the imploding capsule shot and the reference shot [Fig. 1(c)]. Each contour center was corrected from the electrical-pulse propagation that introduced a displacement along the strip. On the reference shot and on the first strip of the capsule shots, the contour centers corresponded to the projection of the initial target position on the diagnostic. For each capsule shot, to correct for differences in diagnostic pointing and initial target center with the reference shot, the contour center array was shifted and magnified to align the contour centers determined on the first strip with the corresponding ones measured on the reference shot. The projected motion of the ablation-front surface at an average radius of 150 μm $(\Delta R_{\rm c})_{150}$ and its associated error dis-

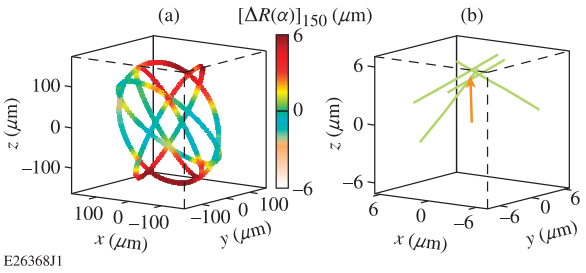

FIG. 2: (a) The four projections of the ablation surface determined at an average radius of 150 μm $\{[R(\alpha)]_{150}\}$ are oriented perpendicular to the lines of sight of the corresponding framing cameras. The color bar shows the variation of the contour radii relative to 150 μm. (b) The 3-D motion of the ablation front surface center at an average radius of 150 μm (orange arrow) corresponds to the point that is at the minimum distance of the four green lines. The lines are defined by the lines of sight of each framing camera shifted by the measured projected motions of the ablation front surface $[(\Delta R_c)_{150}]$. The figures are drawn for the second capsule shot.

tribution was obtained by linearly fitting the evolution of $\Delta R_c|_x$ and $\Delta R_c|_y$ with $\langle R(\alpha)\rangle$ ranging from ~ 300 μm to ~ 100 μm.

The 3-D shape of the ablation-front surface at an average radius of 150 μm was determined by orienting the four projections $[R(\alpha)]_{150}$ perpendicular to the lines of sight of the corresponding framing cameras [Fig. 2(a)]. Because of the 3-D nonuniformities, the centers and averaged radii of the projections were slightly different to the center and averaged radius of the ablation front surface. To account for this, one contour was chosen as a reference and the other contours were shifted transversally and magnified to suppress their radial difference with the reference contour at the two crossing points (i.e., where the polar and azimuthal angles are the same).

The 3-D motion of the ablation front surface center at an average radius of 150 μm (relative to the initial target center) was determined from the four measured projected motions $[(\Delta R_c)_{150}]$. The ablation front surface center was located along the lines defined by the camera lines of sight shifted by the measured projected motions (plus the displacements introduced during the 3-D shape reconstruction process). Therefore, it was obtained by finding the point that is at the minimum distance between the four lines [Fig. 2(b)].

For the three shots, the target modes $l = 1$, 2, and 3 (r_l^m) at an average radius of 150 μm ($\sim$ end of target acceleration) were obtained by decomposing the 3-D shape shifted by the

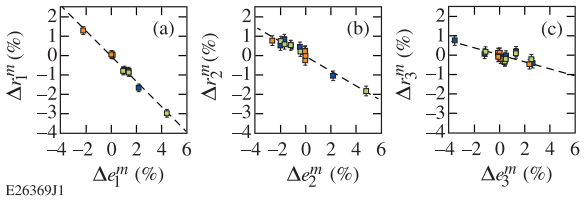

FIG. 3: Difference in the target modes (Δr_l^m) for (a) $l = 1$, (b) $l = 2$, and (c) $l = 3$ of the ablation-front surface between shots 1 and 2 (orange points), 1 and 3 (blue points), and 2 and 3 (green points) as a function of the difference in the corresponding beam energy balance modes (Δe_l^m). The linear fits (dashed black line) and the error bars are plotted.

3-D motion over spherical harmonics [$\overline{R}(\theta_c, \phi_c) = \sum_{l=0}^{3} \sum_{m=-l}^{l} \sqrt{4\pi} r_l^m Y_l^m(\theta_c, \phi_c)$ where $\overline{R}$ is the radius normalized to the averaged radius in percent ($r_0^0 = 100$), (θ_c, ϕ_c) are the polar and azimuthal angles along the oriented contours respectively, $Y_l^m(\theta, \phi)$ are the tesseral spherical harmonics [40], and (θ, ϕ) are the polar and azimuthal angles respectively]. The errors in the modes were evaluated by simulating the error distributions of $(\Delta R_c)_{150}$ and $[\Delta R(\alpha)]_{150}$ and fitting the calculated modes by normal distributions. Errors of $\pm 0.15\%$, $\pm 0.1\%$, and $\pm 0.1\%$ were obtained at the 90th percentile for the modes $l = 1$, 2, and 3, respectively. Systematic errors were evaluated using synthetic self-emission images [41] calculated postprocessing 3-D simulations from ASTER [9] of the second capsule shot. Results showed that the target modes $l = 1$, 2, and 3 reconstructed using the method presented above reproduced the simulated target modes within $\pm 0.04\%$.

The beam-energy balance modes $l = 1$, 2, and 3 (e_l^m) were determined by minimizing $A = \sum_{b=1}^{60} \left(\sum_{l=0}^{3} \sum_{m=-l}^{l} \sqrt{4\pi} e_l^m Y_l^m(\theta_b, \phi_b) - \overline{E}_b \right)^2$ where $\overline{E}_b$ is the energy of the beams normalized to the averaged beam energy in percent ($e_0^0 = 100\%$) and (θ_b, ϕ_b) are the polar and azimuthal angles of the OMEGA beam ports, respectively. The first shot used a typical beam-energy balance with a standard deviation of 2.5%. On the second and third shots, the beam-energy balance was varied to change the modes with a larger variation for modes $m = 0$. The beam energies were measured with integrating spheres within $(\overline{E}_b)_{\rm Err} = \pm 0.5\%$ that were absolutely calibrated within $\pm 2\%$ with calorimeters. This resulted in the same relative error for all modes of $(\overline{E}_b)_{\rm Err}/\sqrt{60} = \pm 0.06\%$.

Figures 3 shows that, for each l, the target modes varied linearly with the beam-energy balance modes with low-mode coupling coefficients ($C_l = \langle \Delta r_l^m / \Delta e_l^m \rangle_l$ where $\langle \rangle_l$ denotes

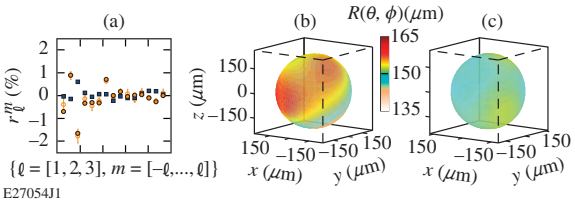

FIG. 4: (a) Comparison of the static target modes (open orange circles) with the target modes obtained for balanced laser (solid orange circle) and optimized beam-energy balance (solid blue squares). Comparison of the target shape reconstructed adding modes l=1, 2, and 3 for balanced laser (b) and optimized beam-energy balance (c).

the average over the points for a given l) of $C_1 = -0.66 \pm 0.05$, $C_2 = -0.38 \pm 0.04$ and $C_3 = -0.18 \pm 0.04$. The strong reduction of C_l with l shows that the lowest modes are the most sensitive to the beam-energy balance. Errors in Δr_l^m of $\pm 0.2\%$, $\pm 0.25\%$, $\pm 0.25\%$ for $l = 1$, 2, and 3 respectively and in C_l (reported above) at the 90th percentile were obtained by comparing the points with their linear fits.

To explain the decrease of C_l with l, the relationship between the laser illumination modes [$\tilde{e}_l^m$ where $\tilde{E}(\theta, \phi) = \sum_{l=0}^{\infty} \sum_{m=-l}^{l} \sqrt{4\pi} \tilde{e}_l^m Y_l^m(\theta, \phi)$, $\tilde{E}(\theta, \phi)$ is the total energy on target per solid angle normalized to $\tilde{e}_0^0 = 100\%$] and the beam energy balance modes was derived [42] following the method described in [43]:

$$\tilde{e}_l^m \approx a_l e_l^m \tag{1}$$

where $a_l = 2\pi \int_{-1}^{1} \tilde{E}_b(\theta, \phi) P_l(\cos\gamma)\, d(\cos\gamma)$ is the single-beam Legendre mode l, $\tilde{E}_b(\theta, \phi)$ is the single-beam energy on target per solid angle normalized to the averaged beam energy, P_l are the Legendre polynomials, and γ is the angle between (θ, ϕ) and (θ_b, ϕ_b). For the phase plates used in the experiment, $a_1 = 0.79$, $a_2 = 0.47$, and $a_3 = 0.2$. Using Eq. (1), an approximately constant coupling of the laser illumination modes to the target modes of $C_l/a_l = -0.85 \pm 0.07$ was obtained showing that the decrease of C_l with l was caused by the beam shapes.

The linear couplings indicate that the target modes are the addition of dynamic modes that evolve linearly with the beam energy balance modes and about constant static modes [$r_l^m = C_l e_l^m + (r_l^m)_{\rm sta}$]. These static modes were evaluated in a second series of four shots. The targets were 863±6-μm-diam., 26.5±0.5-μm-thick CH capsules containing 10 atm of D2. They were irradiated by 100-ps-pickets (overlapped intensity $\sim 1.5 \times 10^{14}$ W/cm^2) to set the

shell's adiabat followed by a 2-ns-long drive pulse (intensity $\sim$ 4.3×10^{14} W/cm^2) that accelerated the target with a total energy of 20.5 ± 1 kJ. The laser focusing and smoothing was kept the same. Two shots were performed with large modes and one using a balanced laser (within $\pm0.9\%$). Figure 4(a) shows the static modes $\langle(r_l^m)_{\rm sta}\rangle_{\rm shots}=\langle r_l^m-C_l e_l^m\rangle_{\rm shots}$ where $\langle\rangle_{\rm shots}$ denotes the average over the three shots [44] with associated errors of $\pm(\sigma_l^m)_{\rm sta}/\sqrt{3}$ where $(\sigma_l^m)_{\rm sta}$ is the standard deviation of $(r_l^m)_{\rm sta}$ over the three shots. The largest static modes were for $l=1$ as they experienced the largest coupling. These static modes, corresponding to the target modes when the laser is balanced, are very close to the modes measured for a balanced laser [Fig. 4(a)].

These results demonstrate that the target modes $l=1$, 2, and 3 can be controlled up to the end of the target acceleration by adjusting the beam-energy balance. On a fourth shot, the target low-modes were reduced by applying (within $\pm1.5\%$) the optimized beam energy balance $(\overline{E}_b)_{\rm opt}=\sum_{l=0}^{3}\sum_{m=-l}^{l}\sqrt{4\pi}(e_l^m)_{\rm opt}Y_l^m(\theta_b,\phi_b)$ where $(e_l^m)_{\rm opt}=-\langle(r_{\rm sta})_l^m\rangle_{\rm shots}/C_l$ to compensate the static modes. Currently, the minimum target modes achievable on OMEGA correspond to the static modes. Figures 4 show that the optimized balance resulted in a further reduction of the target modes $\left\{\left[\sum_{l=1}^{3}\sum_{m=-l}^{l}(r_l^m)^2\right]^{0.5}\right\}$ from 2.3% to 0.8%. Latter in the implosion, the hot-spot pressure rapidly increases (resulting in a rapid start of its x ray emission observed experimentally) and gets much larger than the ablation pressure [45, 46]. Those nonuniformities are no longer amplified by the laser and act as a seed for the nonuniformities at maximum compression [29].

In summary, the target modes l =1, 2, and 3 of directly driven imploding targets were shown, using x-ray tomography, to vary linearly with the beam energy balance modes from approximately constant static modes. This allowed reducing the target low modes from 2.3% to 0.8%. These results are particularly important for direct-drive ICF where the control of the symmetry requires challenging conditions on the laser properties (accurate beam pointing, timing and on-target intensity balance). It shows that even if those conditions are too challenging to diagnose with the current diagnostics on OMEGA, the target symmetry can be controlled by adjusting the beam-energy balance.

This material is based upon work supported by the Department of Energy National Nuclear Security Administration under Award Number DE-NA0001944, the University of Rochester, and the New York State Energy Research and Development Authority. This report was prepared as an account of work sponsored by an agency of the U.S. Government.

---

* Electronic address: tmic@lle.rochester.edu

[1] R. P. Drake, High-Energy-Density Physics: Fundamentals, Inertial Fusion, and Experimental Astrophysics, Shock Wave and High Pressure Phenomena (Springer, Berlin, 2006).

[2] A. L. Kritcher, T. Doeppner, D. Swift, J. Hawreliak, J. Nilsen, J. Hammer, B. Bachmann, G. Collins, O. Landen, C. Keane et al., J. Phys.: Conf. Ser. **688**, 012055 (2016).

[3] R. Nora, W. Theobald, R. Betti, F. J. Marshall, D. T. Michel, W. Seka, B. Yaakobi, M. Lafon, C. Stoeckl, J. A. Delettrez et al., Phys. Rev. Lett. **114**, 045001 (2015).

[4] A. B. Zylstra, J. A. Frenje, P. E. Grabowski, C. K. Li, G. W. Collins, P. Fitzsimmons, S. Glenzer, F. Graziani, S. B. Hansen, S. X. Hu et al., Phys. Rev. Lett. **114**, 215002 (2015).

[5] J. Nuckolls, L. Wood, A. Thiessen, and G. Zimmerman, Nature **239**, 139 (1972).

[6] R. S. Craxton, K. S. Anderson, T. R. Boehly, V. N. Goncharov, D. R. Harding, J. P. Knauer, R. L. McCrory, P. W. McKenty, D. D. Meyerhofer, J. F. Myatt *et al.*, Phys. Plasmas **22**, 110501 (2015).

[7] O. A. Hurricane, D. A. Callahan, D. T. Casey, P. M. Celliers, C. Cerjan, E. L. Dewald, T. R. Dittrich, T. Dppner, D. E. Hinkel, L. F. Berzak Hopkins *et al.*, Nature **506**, 343 (2014).

[8] S. P. Regan, V. N. Goncharov, I. V. Igumenshchev, T. C. Sangster, R. Betti, A. Bose, T. R. Boehly, M. J. Bonino, E. M. Campbell, D. Cao et al., Phys. Rev. Lett. **117**, 025001 (2016).

[9] I. V. Igumenshchev, V. N. Goncharov, F. J. Marshall, J. P. Knauer, E. M. Campbell, C. J. Forrest, D. H. Froula, V. Yu. Glebov, R. L. McCrory, S. P. Regan *et al.*, Phys. Plasmas **23**, 052702 (2016).

[10] P. B. Radha, V. N. Goncharov, T. J. B. Collins, J. A. Delettrez, Y. Elbaz, V. Yu. Glebov, R. L. Keck, D. E. Keller, J. P. Knauer, J. A. Marozas *et al.*, Phys. Plasmas **12**, 032702 (2005).

[11] B. K. Spears, M. J. Edwards, S. Hatchett, J. Kilkenny, J. Knauer, A. Kritcher, J. Lindl, D. Munro, P. Patel, H. F. Robey *et al.*, Phys. Plasmas **21**, 042702 (2014).

[12] S. W. Haan, J. D. Lindl, D. A. Callahan, D. S. Clark, J. D. Salmonson, B. A. Hammel, L. J. Atherton, R. C. Cook, M. J. Edwards, S. Glenzer *et al.*, Phys. Plasmas **18**, 051001 (2011).

[13] A. L. Kritcher *et al.*, Phys. Plasmas **23**, 052709 (2016).

[14] D. S. Clark, C. R. Weber, J. L. Milovich, J. D. Salmonson, A. L. Kritcher, S. W. Haan, B. A. Hammel, D. E. Hinkel, O. A. Hurricane, O. S. Jones *et al.*, Phys. Plasmas **23**, 056302 (2016).

[15] R. L. McCrory, R. E. Bahr, R. Betti, T. R. Boehly, T. J. B. Collins, R. S. Craxton, J. A. Delettrez, W. R. Donaldson, R. Epstein, J. Frenje *et al.*, Nucl. Fusion **41**, 1413 (2001).

[16] V. N. Goncharov, S. P. Regan, E. M. Campbell, T. C. Sangster, P. B. Radha, J. F. Myatt, D. H. Froula, R. Betti, T. R. Boehly, J. A. Delettrez *et al.*, Plasma Phys. Control. Fusion **59**, 014008 (2017).

[17] K. Molvig, M. J. Schmitt, B. J. Albright, E. S. Dodd, N. M. Hoffman, G. H. McCall, and S. D. Ramsey, Phys. Rev. Lett. **116**, 255003 (2016).

[18] C. K. Li, F. H. Sguin, J. A. Frenje, R. D. Petrasso, J. A. Delettrez, P. W. McKenty, T. C. Sangster, R. L. Keck, J. M. Soures, F. J. Marshall *et al.*, Phys. Rev. Lett. **92**, 205001 (2004).

[19] T. J. Murphy, Phys. Plasmas **21**, 072701 (2014).

[20] J. J. Ruby, A. Pak, J. E. Field, T. Ma, B. K. Spears, L. R. Benedetti, D. K. Bradley, L. F. Berzak Hopkins, D. T. Casey, T. Döppner *et al.*, Phys. Plasmas **23**, 072701 (2016).

[21] R. C. Shah, B. M. Haines, F. J. Wysocki, J. F. Benage, J. A. Fooks, V. Glebov, P. Hakel, M. Hoppe, I. V. Igumenshchev, G. Kagan *et al.*, Phys. Rev. Lett. **118**, 135001 (2017).

[22] P. Michel, S. H. Glenzer, L. Divol, D. K. Bradley, D. Callahan, S. Dixit, S. Glenn, D. Hinkel, R. K. Kirkwood, J. L. Kline *et al.*, Phys. Plasmas **17**, 056305 (2010).

[23] G. A. Kyrala, J. L. Kline, S. Dixit, S. Glenzer, D. Kalantar, D. Bradley, N. Izumi, N. Meezan, O. Landen, D. Callahan *et al.*, Phys. Plasmas **18**, 056307 (2011).

[24] R. P. J. Town, D. K. Bradley, A. Kritcher, O. S. Jones, J. R. Rygg, R. Tommasini, M. Barrios, L. R. Benedetti, L. F. Berzak Hopkins, P. M. Celliers *et al.*, Phys. Plasmas **21**, 056313 (2014).

[25] R. Tommasini, S. P. Hatchett, D. S. Hey, C. Iglesias, N. Izumi, J. A. Koch, O. L. Landen, A. J. MacKinnon, C. Sorce, J. A. Delettrez *et al.*, Phys. Plasmas **18**, 056309 (2011).

[26] H. M. Johns, R. C. Mancini, T. Nagayama, D. C. Mayes, R. Tommasini, V. A. Smalyuk, S. P. Regan, and J. A. Delettrez, Phys. Plasmas **23**, 012709 (2016).

[27] D. T. Michel, A. K. Davis, W. Armstrong, R. Bahr, R. Epstein, V. N. Goncharov, M. Hohenberger, I. V. Igumenshchev, R. Jungquist, D. D. Meyerhofer *et al.*, High Power Laser Science and Engineering **3**, e19 (2015).

[28] F. J. Marshall, J. A. Delettrez, R. Epstein, R. Forties, R. L. Keck, J. H. Kelly, P. W. McKenty, S. P. Regan, and L. J. Waxer, Phys. Plasmas **11**, 251 (2004).

[29] I. V. Igumenshchev, D. T. Michel, R. C. Shah, E. M. Campbell, R. Epstein, C. J. Forrest, V. Yu. Glebov, V. N. Goncharov, J. P. Knauer, F. J. Marshall *et al.*, Phys. Plasmas **24**, 056307 (2017).

[30] D. T. Michel, C. Sorce, R. Epstein, N. Whiting, I. V. Igumenshchev, R. Jungquist, and D. H. Froula, Rev. Sci. Instrum. **83** 10E530 (2012).

[31] T. R. Boehly, D. L. Brown, R. S. Craxton, R. L. Keck, J. P. Knauer, J. H. Kelly, T. J. Kessler, S. A. Kumpan, S. J. Loucks, S. A. Letzring *et al.*, Opt. Commun. Commun **133**, 495 (1997).

[32] T. R. Boehly, V. A. Smalyuk, D. D. Meyerhofer, J. P. Knauer, D. K. Bradley, R. S. Craxton, M. J. Guardalben, S. Skupsky, and T. J. Kessler, J. Appl. Phys. **85**, 3444 (1999).

[33] S. Skupsky, R. W. Short, T. Kessler, R. S. Craxton, S. Letzring, and J. W. Soures, J. Appl. Phys. **66**, 3456 (1989).

[34] T. J. Kessler, Y. Lin, J. J. Armstrong, and B. Velazquez, Proc. SPIE **1870**, 95 (1993).

[35] The measured averaged contour radius trajectory is presented in the supplemental material section 1.

[36] D. K. Bradley, P. M. Bell, J. D. Kilkenny, R. Hanks, O. Landen, P. A. Jaanimagi, P. W. McKenty, and C. P. Verdon, Rev. Sci. Instrum. **63** 4813 (1992).

[37] D. T. Michel, V. N. Goncharov, I. V. Igumenshchev, R. Epstein, and D. H. Froula, Phys. Rev. Lett. **111**, 245005 (2013).

[38] D. T. Michel, S. X. Hu, A. K. Davis, V. Yu. Glebov, V. N. Goncharov, I. V. Igumenshchev, P. B. Radha, C. Stoeckl, and D. H. Froula, Phys. Rev. E **95**, 051202(R) (2017).

[39] H. L. Seal, Biometrika **54**, 1 (1967).

[40] E. T. Whittaker and G. N. Watson, *A Course of Modern Analysis* (Cambridge University Press, 1927), p. 392.

[41] A. K. Davis, D. T. Michel, R. S. Craxton, R. Epstein, M. Hohenberger, T. Mo, and D. H.

Froula, Rev. Sci. Instrum. **87** 11E340 (2016).

[42] The derivation of the relationship between the laser illumination modes and the beam energy balance modes is presented in the supplemental material section 2.

[43] S. Skupsky and K. Lee, J. Appl. Phys. **54**, 3662 (1983).

[44] The variation of the absolute values of the target modes as a function of the corresponding laser modes are presented for the first series of shot in the supplemental material section 3.

[45] The experimental observation of the transmission of the ablation front nonuniformities to the inner shell is shows in the supplemental material section 4.

[46] V. N. Goncharov, T. C. Sangster, R. Betti, T. R. Boehly, M. J. Bonino, T. J. B. Collins, R. S. Craxton, J. A. Delettrez, D. H. Edgell, R. Epstein *et al.*, Phys. Plasmas **21**, 056315 (2014).